ACS Photonics

Article

pubs.acs.org/journal/apchd5

Optical Nanoantenna Input Impedance

Yuancheng Xu,[†] Eric Tucker,[‡] Glenn Boreman,[‡] Markus B. Raschke,*[,§] and Brian A. Lail*[,†]

[†]Department of Electrical Engineering, Florida Institute of Technology, Melbourne, Florida, United States

[‡]Department of Physics and Optical Science, University of North Carolina at Charlotte, Charlotte, North Carolina, United States

[§]Department of Physics, Department of Chemistry, and JILA, University of Colorado, Boulder, Colorado, United States

Supporting Information

ABSTRACT: Optical nanoantennas have been studied as a means to manipulate nanoscale fields, local field enhancements, radiative rates, and emissive directional control. However, a fundamental function of antennas, the transfer of power between a coupled load and far-field radiation, has seen limited development in optical antennas owing largely to the inherent challenges of extracting impedance parameters from fabricated designs. As the transitional element between radiating fields and loads, the impedance is the requisite information for describing, and designing optimally, both emissive (transmitting) and absorptive (receiving) nanoantennas. Here we present the first measurement of an optical nanoantenna input impedance, demonstrating impedance multiplication in folded dipoles at infrared frequencies. This quantification of optical antenna impedance provides the long sought enabling step for a systematic approach to improve collection efficiencies and control of the overall antenna response.

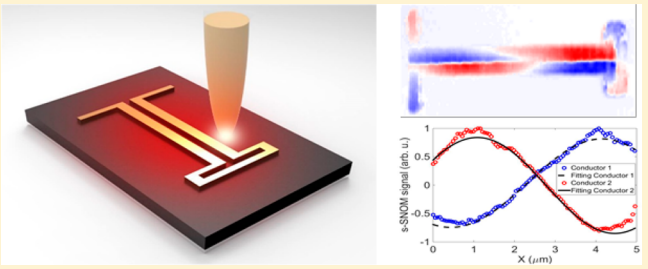

KEYWORDS: *optical nanoantennas, folded dipole antenna, optical antenna impedance, impedance multiplication, infrared frequency*

Advancements in nanofabrication, complemented by a better understanding of light−matter interactions, have led to the development of optical nanoantennas; antennas that exhibit an optical response that enables applications, including surface-enhanced vibrational spectroscopy, nanophotonic phased arrays, imaging, optical communications, and optical metamaterials/metasurfaces.[1−7] Antennas provide a transition between unbounded, radiating electromagnetic fields and the confined local fields associated with the load to the antenna. The load represents systems connected to the antenna terminals, whether for excitation (transmission) or for collection (receiving). A design goal for efficient antenna application is maximal power transfer between the antenna and the load. While certain coupled systems are well-suited to a quantum-optics density-of-states description, an impedance-based approach is applicable.[8,9] Impedance, corresponding to an equivalent circuit representation, is a convenient way to describe the interaction between antenna impedance, Z_A, and the load impedance, Z_L. It is well-known from antenna theory that impedance matching between the load and the antenna, $Z_L = Z_A^*$, corresponds to maximum power transfer.

The significance of the concept of optical antenna impedance is well-established. By defining optical antenna impedance in terms of optical concepts such as local density of states and decay rates, the coupling between the nanoantenna and a quantum emitter can be described.[8] The optical nanocircuit loading effects on radiation and impedance in optical antennas can be formulated, based on circuit theory and numerical simulations.[10−14] Impedance matching properties have been indirectly inferred when describing coupling between optical antennas and waveguides[15−17] as well as through enhanced scattering intensity.[18] However, to the best of our knowledge, a direct measurement and quantification of the impedance of an optical nanoantenna has not yet been performed.

In radiofrequency (RF) operation Ohmic losses in the antenna are often neglected. However, for optical applications, metals have 3 orders of magnitude lower conductivity and, therefore, give rise to large dissipated power, which can exceed the radiated power. In the impedance description, dissipative losses and radiation losses are represented by Ohmic resistance and radiation resistance, respectively. The sum of both is the total input resistance of the antenna corresponding to the real part of the complex input impedance. At resonance the imaginary part of the antenna impedance, that is, the input reactance, is equal to zero. Maximal power transfer requires conjugate matching of antenna and load. Radiation resistance must dominate the antenna impedance in order to overcome the Ohmic dissipation in the antenna. With the large Ohmic loss, this means that radiation efficiency improves as the antenna resistance increases such that radiation becomes the dominant power. This represents a significant deviation from classical antenna design, yet it is a critical requirement for efficient power transfer at optical frequencies.

Folded dipoles for RF applications, designed at the short-circuit resonance, provide a convenient impedance match to

Received: February 22, 2016
Published: April 15, 2016

DOI: 10.1021/acsphotonics.6b00128
ACS Photonics 2016, 3, 881−885

simple transmission lines while maintaining well-behaved directional radiation characteristics.[19] Further, the folded design provides a mechanism for increasing the antenna input impedance, often known as impedance multiplication, through the addition of multiple folded arms. Nanoantenna folded dipoles have been studied through theoretical analysis and simulation, predicting that both the short-circuit and open-circuit terminations provide good radiation characteristics and efficiency.[20]

Here, in order to overcome the limitations of Ohmic loss and to control the antenna impedance in the optical and infrared spectrum, we study several variants of folded dipole antennas: (1) single-folded dipole, (2) single-folded dipole with a stub, (3) double-folded dipole, and (4) triple-folded dipole. The single-folded antenna is the traditional folded dipole design, while the folded dipole with a stub is a variation incorporating an open-circuit coplanar strip line (CPS) stub that transforms to a short-circuit in the antenna arm at operational frequencies while providing electrical isolation for low-frequency load biasing as is often required for detector/sensor applications. With the practical need to achieve optimum antenna efficiency, we determine both short-circuit and open-circuit resonance impedances. Multiple folds are considered at the short-circuit resonance, in order to demonstrate impedance multiplication.

As illustrated in Figure 1, our experiments are performed with the antenna under test (AUT) loading a dipole-coupled

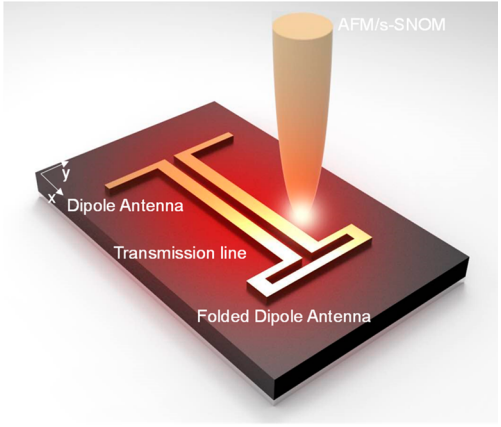

Figure 1. Schematic of *s*-SNOM measurement apparatus.

CPS. The structures are composed of gold and were fabricated on a benzo-cyclobutene (BCB) polymer standoff layer over an aluminum ground plane. The structures were designed for mid-infrared ~10.6 μm (28.3 THz) radiation so that infrared illumination, copolarized with the dipole antenna, couples to a propagating wave on the transmission line. We then use scattering-type scanning near-field optical microscopy (*s*-SNOM), as established previously,[21−25] to measure the superposition of the waves emanating from both the dipole antenna and the folded dipole antenna along the CPS transmission line. More specifically, reflection of the propagating optical wave upon the load at the terminals of the CPS results in a standing wave, where the associated surface-normal $|E_Z|$ near-field component is measured using *s*-SNOM. By fitting the superposition of the standing wave to the measured near-field amplitude and then determining the complex reflection coefficient, the folded dipole antenna impedance is obtained.

The topography (SEM image) and measured near-field amplitude signal can be seen for the dipole-coupled CPS loaded with a single-folded dipole antenna in Figure 2a,b, and a folded

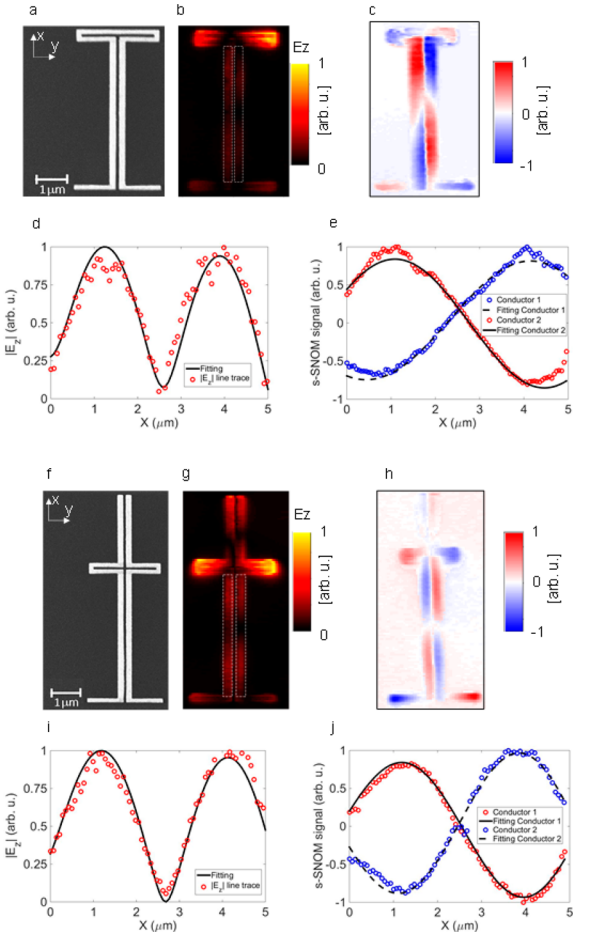

Figure 2. SEM image of the antenna coupled CPS with (a) a folded dipole antenna and (f) a folded dipole antenna with a stub for DC isolation, where conductor 1 is on the right side and conductor 2 is on the left side. Experimental near-field images show the amplitude signal along the CPS with (b) a folded dipole antenna and (g) a folded dipole with a stub designed at the short-circuit resonance. Experimental near-field results show surface wave with phase variation on the CPS with (c) a folded dipole and (h) a folded dipole with a stub at open-circuit resonance. (d, i) Analytical fitting to the corresponding measured amplitude signals. (e, j) Analytical fitting to the corresponding measured data with phase variation.

dipole antenna with a stub in Figure 2f,g at their short-circuit resonances. The magnitude of the vertical $|E_Z|$ is found by $\mathrm{Re}(E_Z) = |E_Z| \cos(\varphi_Z)$, where $|E_Z|$ is the near-field amplitude and φ_Z is the phase.[26,27] The near-field amplitude signal $|E_Z|$ in this measurement configuration can be observed in the line scan plots in Figure 2d,i, showing the standing wave along the CPS transmission line. In order to visualize the distribution of the surface near-field phase variation at the open-circuit resonance at λ = 10.6 μm, φ_Z is shown in Figure 2c,h. The corresponding open-circuit model line scan analysis along the CPS lines are shown in Figure 2e,j. We also investigate the impedance multiplication for the IR antenna at the short-circuit resonance by using near-field measurements. In Figure 3a,c, the SEM images are shown for the double- and triple-folded dipole antennas designed at the short-circuit resonance. The

DOI: 10.1021/acsphotonics.6b00128
ACS Photonics 2016, 3, 881−885

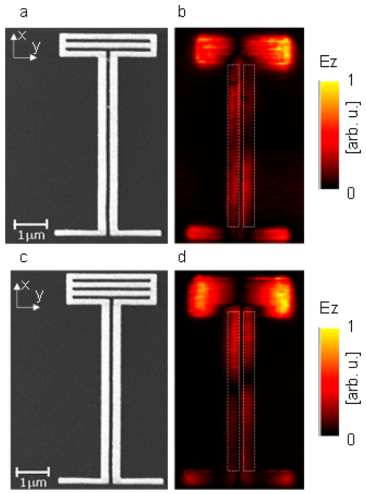

Figure 3. SEM images of (a) double-folded dipole antenna and (c) triple-folded dipole antenna. Measured *s*-SNOM signals along CPS for (b) double-folded dipole antenna and (d) triple-folded dipole antenna.

corresponding near-field amplitude $|E_Z|$ along the conductors are presented in Figure 3b,d.

The magnitude of E_Z along the transmission line represents a standing wave, which results from the interference of optical wave coupling into the CPS from the dipole antenna end and the load antenna end. This superposition is described by a geometric-series expansion to account for all the reflections at the impedance mismatched loads (eq 4, Supporting Information). A nonlinear fitting algorithm that minimized the sum of squares errors was applied to the measured s-SNOM signal line traces, as shown in Figure 2d,I for the folded dipole with and without a stub at the short-circuit resonance and Figure 2e,j for the open-circuit resonance. Note that the red data points in Figure 2d,I represent the variation of the near-field amplitude signal along the length of the CPS, averaged about the width of the CPS, contained within the white box shown in Figure 2b and g, respectively. The impedance of the AUT can be determined from the reflection expression (eq 7, Supporting Information). There is a slight asymmetry in the s-SNOM signal, especially in regard to the location of the nodes, as seen in Figures 2 and 3, which is attributed to the tilting of the orientation of the structure with respect to the incident beam. One can also see that the fit deviates slightly from the measured data near the ends of the CPS. This deviation is because the analytical expression assumes an abrupt termination at each terminal of the transmission line, while in the real fabrication and measurement both the dipole antenna and the folded dipoles provide field continuity at the physical connection with the CPS. The resulting experimental values including estimates of their uncertainties based on the above considerations, are summarized in Table 1.

As seen in Table 1, the impedance prediction for the folded dipole antennas with and without a stub at both the short-circuit resonance and open-circuit resonance from simulation and measurement are in good agreement. The simulated input impedance is computed by directly exciting the antenna at the feed gap in a driven model from Ansys HFSS (Supporting Information, Numerical Method of driven model), while measured results are extracted from near-fields, as described above. For comparison, simulations of a single gold dipole of similar line width predict input impedances of 83.5 Ω (free space), 73.5 Ω (BCB half-space substrate), and 54.6 Ω (BCB substrate on Al ground plane). The input impedance values of the multielement folded dipole antennas are also listed in Table 1 in comparison with those of the single-folded dipole antennas. Note that the increase of the input impedance for the triple-folded dipole compared to the double-folded dipole is much smaller than the difference between the single-folded and double-folded dipole antenna which can be attributed to the IR metal loss and the increased electrical width of the folded structure.

Table 1. Impedance Comparison between Measurement and Simulation Results for the Folded Dipole Antenna with and without a Stub and Multi-Element Folded Dipole Antenna

	Short-circuit resonance		Open-circuit resonance	
	Experiment (kΩ)	Simulation (kΩ)	Experiment (kΩ)	Simulation (kΩ)
	0.193 ± 0.010	0.189	0.679 ± 0.034	0.667
	0.178 ± 0.009	0.175	0.653 ± 0.033	0.639
	0.264 ± 0.013	0.270	-	-
	0.290 ± 0.029	0.334	-	-

The differences between simulation and measured impedance values is due to the aforementioned deviation in the analytical fitting of the measured data. Another factor is small but unavoidable perturbations of the antenna near-field through the s-SNOM tip. Also, with increasing structural complexity of the antennas with increasing number of folds, the fabrication imperfections in length and width are compounded and may account for some of the corresponding increase in deviation between experiment and theory. However, except for the triple-folded, which is the most complex geometry investigated, all experimental values are within their uncertainties well predicted by the simulations, with in part excellent agreement, especially for the simpler geometries.

An impedance-based description of optical nanoantenna/load interactions provides a convenient framework for design and characterization. Coupling between two-level systems and optical antennas has been described through circuit theory.[8] Lumped element nanocircuit descriptions for specific canonical structures such as nanospheres,[10,11] nanorods,[28] split-ring resonators,[29,30] and flat metallic surface plasmons[31] have been reported. For simple geometries it is possible to use analytical models to predict impedance. However, a pragmatic approach to the design of impedance-matched optical nanoantennas/loads is contingent on the ability to experimentally assess impedance of arbitrary loads and nanoantennas.

Here we have, for the first time, presented the experimental determination of optical nanoantenna impedance. Empirical demonstration of impedance multiplication in folded dipole nanoantennas reveals the feasibility of impedance tuning in optical nanoantennas. The targeted increase in input impedance provides a means of overcoming metallic losses such that the interaction between radiative resistance and load is the dominant coupling mechanism. The experimental techniques that are presented are applicable to arbitrary antenna designs and loads so that the design space is not constrained, therefore complex geometries and impedance matching networks are attainable.

DOI: 10.1021/acsphotonics.6b00128
ACS Photonics 2016, 3, 881−885

In summary, through the excitation of stable standing waves on transmission line coupled antennas, we have achieved a systematic way to determine the impedance values of optical and infrared antennas through near-field imaging and analysis. To the best of our knowledge, this represents the first direct realization of an input impedance measurement at optical frequencies. Both open and short-circuit resonances, as well as multielement antennas, have been investigated to present a blueprint for maximizing collection efficiency and flexibly controlling nanoantenna impedance through design as a means of achieving maximum power transfer through impedance matching. This work provides a requisite step toward extending all theoretical concepts of optical and infrared nanoantennas into practical applications by demonstrating the measurement of well-controlled input impedance in optical nanoantennas.

METHODS

Sample Fabrication. The folded CPS structures (with and without a stub) were composed of gold and were fabricated on an aluminum ground plane with benzo-cyclobutene (BCB) polymer (Dow Cyclotene 3022−35 resin) used as the standoff layer. Briefly, the ground plane was formed by depositing 150 nm of aluminum onto a cleaned silicon wafer using e-beam evaporation. Next, a 1.2 um thick BCB layer was deposited by spin coating the resin onto the sample, then a hard cure was done in a nitrogen environment. The structures were patterned in poly(methyl methacrylate) (PMMA) resist using e-beam lithography, which was followed by development of this resist, metallization, and lift-off using Remover PG to yield 110 nm thick structures. The conductors of the CPS are 5 μm long, 220 nm wide, and are separated by 110 nm.

Near-Field Microscopy Set-up. Near-field measurements were performed utilizing a custom-built s-SNOM, which operates utilizing a homodyne detection scheme. The instrument has a layout as shown in Figure 1, and a CO_2 laser operating at a wavelength of 10.6 μm was used as the source and is directed toward a 50/50 beam splitter (BS). A portion of the s-polarized incident beam is then reflected toward the sample while a comparable fraction is directed into a reference path. The reflected beam is focused onto the sample on the AFM stage at an angle of 60° off-normal using an off-axis parabolic reflector (OAP), which excites the structures of interest. The AFM, operating under tapping mode at 240−280 kHz, scatters predominantly p-polarized light from these excited near-fields back toward the beam splitter. The other portion of the incident beam at the beam splitter is directed toward a reference mirror (RM) in the reference path where it passes through a quarter wave plate (QWP). Then, this reference beam is reflected back toward the beam splitter where it is combined with the scattered near-field radiation. The interferometric homodyne signal mainly corresponding to the E_Z field is measured by a liquid nitrogen cooled Mercury Cadmium Telluride (MCT) detector. A lock-in amplifier is used to measure the signal at the second harmonic of the tip oscillation. Wire grid polarizers (WG) are utilized to enable cross polarized excitation and detection. In a region of interest, AFM scans are made at different reference mirror positions. A cosine function is fit point-by-point across these images, which allows for determination of amplitude and phase of the near-field signal.

Numerical Calculations. The simulation results in Table 1 were computed numerically using Ansys HFSS, which is based on the finite element method (http://www.ansys.com). Lumped port excitations in driven models are used to directly compute the feed gap voltage/current, hence the input impedance, of the folded dipole antennas (Supporting Information, Numerical Method of driven model). For all simulation designs, we use dispersive material properties for gold, aluminum and BCB measured by the infrared variable-angle spectroscopic ellipsometry (IR-VASE).

ASSOCIATED CONTENT

Supporting Information

The Supporting Information is available free of charge on the ACS Publications website at DOI: 10.1021/acsphotonics.6b00128.

Mathematical equations pertaining to the fitting of the standing wave on the CPS line coupled to the dipole antenna and load antenna. Numerical method setup of folded dipole antenna in driven model analysis in Ansys HFSS. Analytical fitting to the measured data of double-folded and triple-folded dipole antenna. (PDF)

AUTHOR INFORMATION

Corresponding Authors

*E-mail: blail@fit.edu.

*E-mail: Markus.Raschke@Colorado.EDU.

Notes

The authors declare no competing financial interest.

ACKNOWLEDGMENTS

The authors acknowledge Navaneeth Premkumar of the Applied and Computational Electromagnetics Lab at Florida Institute of Technology for valuable insight and discussions. This work has been supported by the National Science Foundation (Grant 1204993).

REFERENCES

(1) Adato, R.; Aksu, S.; Altug, H. Engineering Mid-Infrared Nanoantennas for Surface Enhanced Infrared Absorption Spectroscopy. *Mater. Today* **2015**, *18*, 436−446.

(2) Sun, J.; Timurdogan, E.; Yaacobi, A.; Hosseini, E. S.; Watts, M. R. Large-Scale Nanophotonic Phased Array. *Nature* **2013**, *493*, 195−199.

(3) Monticone, F.; Alu, A. Leaky-Wave Theory, Techniques, and Applications: From Microwaves to Visible Frequencies. *Proc. IEEE* **2015**, *103*, 793−821.

(4) Dregely, D.; Lindfors, K.; Lippitz, M.; Engheta, N.; Totzeck, M.; Giessen, H. Imaging and Steering an Optical Wireless Nanoantenna Link. *Nat. Commun.* **2014**, *5*, 4354.

(5) Yu, N.; Capasso, F. Flat Optics with Designer Metasurfaces. *Nat. Mater.* **2014**, *13*, 139−150.

(6) Singh, A.; Hugall, J. T.; Calbris, G.; van Hulst, N. F. Fiber-Based Optical Nanoantennas for Single-Molecule Imaging and Sensing. *J. Lightwave Technol.* **2015**, *33*, 2371−2377.

(7) *Optical Antennas*, 1 ed.; Agio, M., Alù, A., Eds.; Cambridge University Press: Cambridge, 2013.

(8) Greffet, J.-J.; Laroche, M.; Marquier, F. Impedance of a Nanoantenna and a Single Quantum Emitter. *Phys. Rev. Lett.* **2010**, *105*, 117701.

(9) Olmon, R. L.; Raschke, M. B. Antenna−load Interactions at Optical Frequencies: Impedance Matching to Quantum Systems. *Nanotechnology* **2012**, *23*, 444001.

(10) Engheta, N.; Salandrino, A.; Alù, A. Circuit Elements at Optical Frequencies: Nanoinductors, Nanocapacitors, and Nanoresistors. *Phys. Rev. Lett.* **2005**, *95*, n/a.

(11) Engheta, N. Circuits with Light at Nanoscales: Optical Nanocircuits Inspired by Metamaterials. *Science* **2007**, *317*, 1698−1702.
(12) Alù, A.; Engheta, N. Tuning the Scattering Response of Optical Nanoantennas with Nanocircuit Loads. *Nat. Photonics* **2008**, *2*, 307−310.
(13) Alù, A.; Engheta, N. Input Impedance, Nanocircuit Loading, and Radiation Tuning of Optical Nanoantennas. *Phys. Rev. Lett.* **2008**, *101*, n/a.
(14) Alu, A.; Engheta, N. Theory, Modeling and Features of Optical Nanoantennas. *IEEE Trans. Antennas Propag.* **2013**, *61*, 1508−1517.
(15) Huang, J.-S.; Feichtner, T.; Biagioni, P.; Hecht, B. Impedance Matching and Emission Properties of Nanoantennas in an Optical Nanocircuit. *Nano Lett.* **2009**, *9*, 1897−1902.
(16) Wen, J.; Romanov, S.; Peschel, U. Excitation of Plasmonic Gap Waveguides by Nanoantennas. *Opt. Express* **2009**, *17*, 5925.
(17) Fang, Z.; Fan, L.; Lin, C.; Zhang, D.; Meixner, A. J.; Zhu, X. Plasmonic Coupling of Bow Tie Antennas with Ag Nanowire. *Nano Lett.* **2011**, *11*, 1676−1680.
(18) Liu, N.; Wen, F.; Zhao, Y.; Wang, Y.; Nordlander, P.; Halas, N. J.; Alù, A. Individual Nanoantennas Loaded with Three-Dimensional Optical Nanocircuits. *Nano Lett.* **2013**, *13*, 142−147.
(19) Balanis, C. A. *Wiley: Advanced Engineering Electromagnetics*, 2nd ed.; Wiley: New York, 2012 (accessed Nov 17, 2015).
(20) Iizuka, H.; Engheta, N.; Fujikawa, H.; Sato, K. Arm-Edge Conditions in Plasmonic Folded Dipole Nanoantennas. *Opt. Express* **2011**, *19*, 12325.
(21) Yang, H. U.; Olmon, R. L.; Deryckx, K. S.; Xu, X. G.; Bechtel, H. A.; Xu, Y.; Lail, B. A.; Raschke, M. B. Accessing the Optical Magnetic Near-Field through Babinet's Principle. *ACS Photonics* **2014**, *1*, 894−899.
(22) Schnell, M.; García-Etxarri, A.; Huber, A. J.; Crozier, K.; Aizpurua, J.; Hillenbrand, R. Controlling the near-Field Oscillations of Loaded Plasmonic Nanoantennas. *Nat. Photonics* **2009**, *3*, 287−291.
(23) Olmon, R. L.; Rang, M.; Krenz, P. M.; Lail, B. A.; Saraf, L. V.; Boreman, G. D.; Raschke, M. B. Determination of Electric-Field, Magnetic-Field, and Electric-Current Distributions of Infrared Optical Antennas: A Near-Field Optical Vector Network Analyzer. *Phys. Rev. Lett.* **2010**, *105*, 167403.
(24) Schnell, M.; Alonso-González, P.; Arzubiaga, L.; Casanova, F.; Hueso, L. E.; Chuvilin, A.; Hillenbrand, R. Nanofocusing of Mid-Infrared Energy with Tapered Transmission Lines. *Nat. Photonics* **2011**, *5*, 283−287.
(25) Krenz, P. M.; Olmon, R. L.; Lail, B. A.; Raschke, M. B.; Boreman, G. D. Near-Field Measurement of Infrared Coplanar Strip Transmission Line Attenuation and Propagation Constants. *Opt. Express* **2010**, *18*, 21678−21686.
(26) Jones, A. C.; Olmon, R. L.; Skrabalak, S. E.; Wiley, B. J.; Xia, Y. N.; Raschke, M. B. Mid-IR Plasmonics: Near-Field Imaging of Coherent Plasmon Modes of Silver Nanowires. *Nano Lett.* **2009**, *9*, 2553−2558.
(27) Olmon, R. L.; Krenz, P. M.; Jones, A. C.; Boreman, G. D.; Raschke, M. B. Near-Field Imaging of Optical Antenna Modes in the Mid-Infrared. *Opt. Express* **2008**, *16*, 20295.
(28) Huang, C.; Yin, X.; Huang, H.; Zhu, Y. Study of Plasmon Resonance in a Gold Nanorod with an LC Circuit Model. *Opt. Express* **2009**, *17*, 6407.
(29) Ishikawa, A.; Tanaka, T.; Kawata, S. Negative Magnetic Permeability in the Visible Light Region. *Phys. Rev. Lett.* **2005**, *95*, 237401.
(30) Zhou, J.; Koschny, T.; Kafesaki, M.; Economou, E. N.; Pendry, J. B.; Soukoulis, C. M. Saturation of the Magnetic Response of Split-Ring Resonators at Optical Frequencies. *Phys. Rev. Lett.* **2005**, *95*, 223902.
(31) Staffaroni, M.; Conway, J.; Vedantam, S.; Tang, J.; Yablonovitch, E. Circuit Analysis in Metal-Optics. *Photonics Nanostructures - Fundam. Appl.* **2012**, *10*, 166−176.

DOI: 10.1021/acsphotonics.6b00128
ACS Photonics 2016, 3, 881−885